# Dalton Transactions

Accepted Manuscript






ROYAL SOCIETY OF CHEMISTRY

www.rsc.org/dalton

Journal Name

ARTICLE

# Novel fractional crystallization route to porous $TiO_2$-$Fe_2O_3$ composites: large scale preparation and high performances as photocatalyst and Li-ion battery anode

Received 00th January 20xx,
Accepted 00th January 20xx

DOI: 10.1039/x0xx00000x

www.rsc.org/

Li Li,[a] Jianbo Zhang[b] and Qingshan Zhu[a,*]

Meso/macroporous $TiO_2$-$Fe_2O_3$ composite particles are prepared using naturally abundant ilmenite via a novel heat treatment induced fractional crystallization strategy in fluidized bed. Fluid-bed roasting in oxidizing and reducing environments is carried out in order respectively to realize the fractional crystallization of ilmenite. Subsequently, acid leaching is employed to remove most of the ferrous phase and form porous $TiO_2$-$Fe_2O_3$ composites. The influences of the reaction parameters on the composition, structure and properties of the products are studied. It is found that the pore structure and composition of the porous $TiO_2$-$Fe_2O_3$ composite particles can be controlled simply by controlling some parameters, such as the roasting time, temperature, precursor particle size, and post-roasting treatment. Photocatalytic and electrochemical cycling measurements show that the synergism of porous structure and the controlled doping of α-$Fe_2O_3$ endow the as-obtained products excellent visible light photocatalytic activity and enhanced performance in lithium ion battery. The composite porous particles thus obtained may have some promising applications in the fields of photocatalyst, electrode materials, absorbers and pigments etc. This work opens a new avenue for reasonable combination of cost-effective raw material, large scale fabricating process and fine control over the structure and composition in the design and preparation of functional materials.

## Introduction

In the past decades, the design, preparation and modification of porous $TiO_2$ have attracted enormous interests[1-4], for the presence of pores usually leads to higher surface area and more active sites, which endow these porous $TiO_2$ materials improved properties and wider application potential in various fields such as photocatalysis, photovoltaics, electrical energy storage and so on[5-8]. However, till now, the application of porous $TiO_2$ materials is still limited by two facts. First, the performance of $TiO_2$ is under the thumb of its low quantum efficiency, narrow spectral response frequency band (ultraviolet, for its high band gap) and low electric capacity[9]. Second, the fabrication of porous $TiO_2$ and fine control over their pore structures are highly dependent on the employment of well-selected assistants[10-14], which inevitably increases the cost and the complexity of the synthetic process (for the elimination of the assistants after the formation of the pores) and, more importantly, brings unfavorable influences to the composition and pore structure[15-17]. To further improve the economical efficiency and the performance of porous $TiO_2$ materials, new strategies and formation mechanisms which can achieve fine control over the pore structure and composition through economically affordable fabricating process need to be explored in more detail.

To improve the quantum efficiency of $TiO_2$, increasing the crystallinity has been proved to be a reasonable and effective way[18].The commonly used "bottom-up" strategies for porous $TiO_2$ structures usually involve the use of organic surfactants as templates for the formation of pores[10-14], and heat treatment temperature is limited in relatively low degree to avoid the collapse of the pores[10,19]. Therefore, the porous structures thus obtained possess low crystallinity and high degree of lattice defect, which may hamper the electron and ion transfer, and lead to inferior performance[20-21]. Comparatively, the employment of heat treatment induced fractional crystallization of inorganic reaction system, which has been long-term used to obtained the porous glass materials[22-23], is a promising candidate for the fabrication of porous structures with higher crystallinity and less lattice defect, for the fractional crystallization is usually carried out by high temperature heat treatment. The main challenge of this fractional crystallization strategy currently is the establish of reliable heat treatment process to realize fine control over the crystallization and phase distribution. On the other hand, for the broadening of the spectral response frequency band and the enhancement electric capacity, controlled modifying of

[a] State Key Laboratory of Multiphase Complex Systems, Institute of Process Engineering, Chinese Academy of Sciences, Beijing, 100190, China.
[b] Pangang Group Research Institute Co.,ltd.,Panzhihua, 61700, China.

†Electronic Supplementary Information (ESI) available: [Integrated characterizations of the Panzhihua ilmenite particles, Schematic of the fluidized bed reactor, Deconvolution of XRD patterns of sample S1, SEM and TEM images of sample S2, XRF bar chart and chemical compositions table, XRD patterns of the contrast samples, low-magnification back-scattered electron images of samples, UV–vis diffusive reflectance spectra, Optical band gap energy and XPS data, X-ray photoelectron spectra, The first discharge–charge cycling plots, discharge capacities and Coulombic efficiencies.]. See DOI: 10.1039/x0xx00000x

$TiO_2$ with metal, metal oxide or other elements is commonly employed[24-27]. Among which the combination of $Fe_2O_3$ and $TiO_2$ has been proved to be an effective way to extend the spectral response frequency band (when used as photocatalyst)[24,28-29] and increase the electric capacity (when used as electrode material) of $TiO_2$[30-31]. To effectively enhance the electron and ion transfer of $TiO_2/Fe_2O_3$ composites, the major precondition is that the two phases should be connected via coherent interphase with low defect level, to achieve which an extra crystal reconstruction treatment is commonly necessary[32-33]. However, the reconstruction treatment usually leads to tedious preparation process and increased cost. Currently, to improve both the performance and the economic efficiency of porous $TiO_2/Fe_2O_3$ composites, it is of great importance to develop simple, reliable and industrial acceptable routes to realize controlled fractional crystallization of low-cost reactants and achieve high crystallinity and coherent interphase with low defect level.

Herein, we have successfully developed a fluid-bed roasting induced fractional crystallization process for the controlled preparation of $TiO_2/Fe_2O_3$ composites with naturally abundant ilmenite as low-cost starting material. Fluid-bed treatment holds the advantages of uniform thermal and mass transfer, easy control, being beneficial to large scale preparation et al[34-35]. Ilmenite is naturally formed mineral, in addition to its low cost, a more important nature is the uniform distribution of Fe and Ti elements, which is favorable to the formation of high crystallinity and coherent interphase with low defect level of the $TiO_2/Fe_2O_3$ composites. The influences of some parameters, such as the roasting time, temperature, particle size of the ilmenite precursor, and post-roasting treatment on the pore structure and composition of the products have been investigated. In addition, the photocatalytic performance and electrochemical behavior as anode for lithium ion battery of the porous $TiO_2/Fe_2O_3$ composites have been measured, both of which show remarkably improvement and great dependence on the special pore structure, crystallinity, and composition.

## Experimental Section

**Materials.** The ilmenite concentrate is provided by the Panzhihua Iron and Steel Group Corporation (Sichuan, China). The as-received ilmenite is sieved; only particles in the 50-75μm size range are used during the study. The ilmenite primarily contains hexagonal $FeTiO_3$, as illustrated by the XRD pattern in Fig. S1. The chemical composition of the ilmenite is summarized in Table S1; All the gases ($H_2$, $N_2$, and dry air) used in the thermal pretreatment experiments are purchased from Beijing HuaYuan Gas Chemical Industry Co., Ltd (Beijing, China). Among them, the purity of both the $H_2$ and $N_2$ are 99.999%. Degussa P25 (a commercial titania products with both anatase and rutile phases) is purchased from Shanghai Haiyi Scientifc & Trading Co., Ltd. Hydrochloric acid, polyvinylidenedifluoride (PVDF) and methyl blue (MB) are all of analytical grade and purchased from Beijing Chemical Factory.

Table 1 Experimental conditions and parameters of the products.

| Sample | Reduction time / min | I(101) /I(110) | The surface area($m^2g^{-1}$) | Pore volumes |
|---|---|---|---|---|
| S1 | 5 | 0.63 | 42.1 | 0.45 |
| S2 | 15 | 0.67 | 76.5 | 0.47 |
| S3 | 30 | 0.61 | 51.2 | 0.46 |
| S4 | 0 | — | — | — |
| S5 | 40 | — | — | — |

The electrolyte solution with 1 M LiPF6/ethylene carbonate (EC)/diethyl carbonate(DMC)/ethyl methyl carbonate (EMC) (1:1:1 by volume) is purchased from Guangzhou Tinci Materials Technology Co., Ltd. Deionized water is used for all experiments. Deionized water is used in all experiments.

**Synthesis of porous $TiO_2$-$Fe_2O_3$ composites.** The oxidation and reduction thermal pretreatments are carried out in a fluidized bed reactor composed of a quartz tube (Fig. S2) with a perforated plate for gas distribution. In each experiment, 10g ilmenite powders is placed into the reactor and preheated in fluidization by the shielding gas at a flow rate of about 0.4 L/min. When the desired temperature is achieved, the fluidization gas is changed to the reaction gas. After a certain period of heating, a rapid cooling with the shielding gas is carried out before the powders are taken out of the reactor. To obtained the $TiO_2$ network, the ilmenite is oxidized in air at 800℃for 40 min. The as-oxidized ilmenites are subjected to a reduction pretreatment at 600℃ for 5-30 min to tuning the porosity and component of the $TiO_2$ network (see Table 1).

In the subsequent leaching experiments, the pre-treated ilmenite samples is added to a beaker with 40 mL 20% HCl solution to obtain a mixture with liquid to solid ratio of 4 mL/g. Then the mixture is transferred into a Teflon-lined stainless-steel autoclave to be hydrothermally treated at 145℃, and after 5h, porous $TiO_2$-$Fe_2O_3$ composites are obtained. The solid products prepared are washed by hot 10g/L NaOH solution and deionized water several times and dried in air at room temperature.

**Characterization.** The scanning electron microscopy (SEM) images and energy dispersive X-ray (EDX) spectrum of the samples are obtained using a Quanta 200 microscope and EMAX Horiba, respectively. Cross-sections are prepared by mounting particles in epoxy and grinding with successively finer diamonds. The final lap used 1-μm diamond. Axios max X-ray fluorescence (XRF) spectroscope is used for chemical composition analysis. Transmission electron microscopy (TEM) and High-resolution TEM(HRTEM) analysis are obtained on a JEM-2100F electron microscope. The XRD patterns of the catalysts are recorded on a PANalyticalX'Pert MPD Pro X-ray diffractometer using Cu-Kα radiation source (λ=0.154056 nm). The XRD patterns are used to identify the crystal phase, ratio of Rutile (101) to Rutile (110), and crystallite size. Due to the overlap of the rutile (101) peak with hematite (120), a numerical deconvolution technique is used to separate these peaks (Fig. S3)[36]. Brunauer-Emmett-Teller (BET) measurements are performed on Micrometrics ASAP 2020 spectrometer.

XPS measurements are made with a PHI Quantera SXMX spectrometer with an Mg-Kα source (1253.6 eV). The samples are analyzed at pressures less than $10^{-7}$ Pa. Binding energies are measured for O1s, Ti2p, and Fe2p. The C1s binding energy of 284.8 eV was taken as the standard for correction of experimental binding energies. The O/Ti/Fe atomic ratios are also given by the XPS measurements.

UV/Vis absorption spectra for the dry pressed disk of the samples are obtained by using a UV/Vis spectrophotometer (Varian Cary5000), which is used to calculate the optical band energy of the samples[36]. Absorption spectra are referenced to $BaSO_4$.

**Photodegradation of methyl blue.** 45 mg photocatalyst is added to 45 mL $4*10^{-5}$ M MB solution and sonicated for 20 min. The pH value of the suspension is adjusted to 3.0 using 1M HCl (aq). The reaction system is stirred in dark for 30 min to reach the adsorption equilibrium of MB and then exposed to UV light from a high-pressure Hg lamp(100 W). At a certain interval, 3 ml of the mixture is drawn from the system, centrifuged and then the absorption spectrum of the dye is monitored by a Shimadzu UV-1601 spectrophotometer. The degradation reaction is timed from the lighting of the high pressure Hg lamp.

**Characterization of the As-Obtained porous $TiO_2$-$Fe_2O_3$ compisites in a Lithium Ion Battery.** For fabrication of the working electrodes, the as-prepared powders are mixed with acetylene black and polyvinylidene fluoride (PVDF) in weight ratio of 80:10:10 in N-methyl-2 pyrrolidinon (NMP). The obtained slurry is coated onto Cu foil and dried at 80℃ for 4h. Then, the dried tape is punched into round plates with diameter of 10.0mm as the cathode electrodes. The electrodes are dried again at 120℃ for 5h in a vacuum prior to use. Finally, the prepared anodes and Celgard 2400 separator (diameter of 16.0mm) are placed into an argon atmosphere filled glove box ($H_2O$ and $O_2$<1ppm) and assembled into a coin cell (CR2032) with lithium cathode, electrolyte of 1M $LiPF_6$ in EC-DEC-DMC (1:1:1 vol.%) and the other components of the coin-type cell. The cells are charged and discharged at the current density of 0.2mA•cm-2 on a battery tester in the voltage of 1.0-3.0V at room temperature.

## Results and Discussion

The $TiO_2$-$Fe_2O_3$ composite products are prepared via heat treatment induced fractional crystallization using fluid-bed reactor (Fig. 1a). As fluid-bed reactors are sophisticated roasting equipment that has been widely employed in industrial production[17-18], the strategy for controlled preparation of $TiO_2$-$Fe_2O_3$ composites we reported here, with properly optimized parameters, has strong potential to be expanded for large scale production. The typical cross-section SEM images with different magnifications of sample S2 are shown in Fig. 1c-d. A panoramic image of Fig. 1c indicates the porous $TiO_2$-$Fe_2O_3$ composite particles with a similar size (average center diameter of 50-75μm) and shape to the pulverized ilmenite powder (also see Fig.S1a-b and S4a). From a magnified image show in Fig. 1c inset, it can be seen clearly

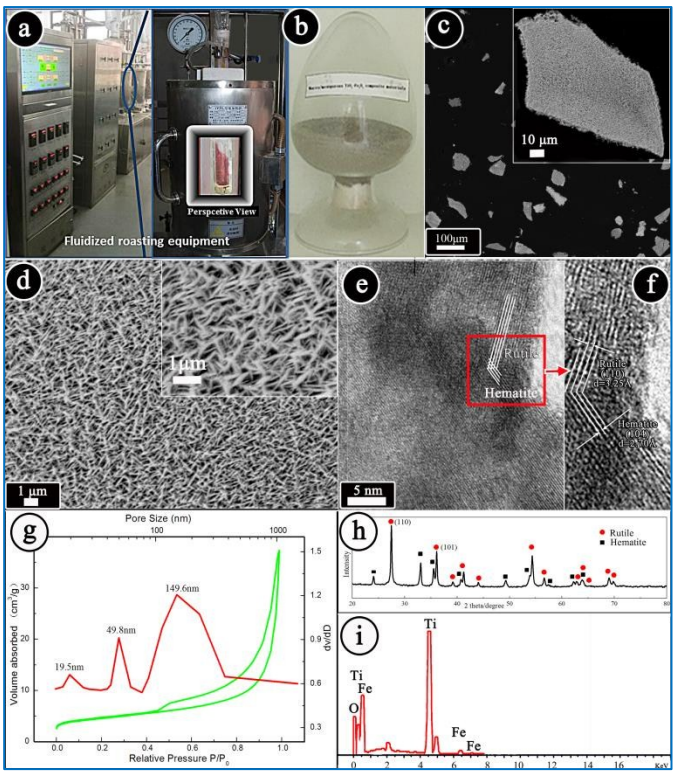


Fig. 1 Integrated characterizations of the as-obtained meso-macroporous $TiO_2$-$Fe_2O_3$ composite particles (Sample S2 in Table 1) (a) Photographs of the fluidized roasting equipment, (b) Photographs of the product, (c–d) SEM images of the cross-section of the sample at different magnifications, (e–f) HRTEM images with different magnifications (the Fig. f is the magnified image of the selected areas marked by the red squares), (g) Nitrogen adsorption–desorption isotherms and the corresponding pore size distribution of the sample, (h)XRD spectra of the sample, (i)EDX spectra of the sample.

that the pores distribute uniformly in the whole particle. The high-magnification observation on the cross section demonstrates that the composite particles exhibit hierarchical meso-macro porous structure with the pore size range of 50-180 nm (Fig. 1d and inset), and the walls of the porous particles are assembled by lamellate $TiO_2$ crystals (also see Fig. S4b-d). To further reveal the fine structure of the composite porous particles, TEM analysis is also carried out. As shown in Fig. S4c, the TEM confirms the existence of 10–50 nm pore. The corresponding HRTEM image is show in Fig. 1e, from which two different crystal lattices can be seen: the wider one represents rutile and the narrower one represents hematite, with lattice plane spacing of ca. 0.276 nm and ca. 0.174 nm, respectively. The clear and regular lattice image demonstrates the high crystallinity feature of the products, which can also be proved by the existence of coherent grain boundary (Fig. 1f).

In order to study the BET surface areas and internal pore structures of the products, the nitrogen adsorption-desorption measurements are carried out (Fig. 1g). The product possesses a type IV $N_2$ adsorption-desorption isotherm with the D kind hysteresis loop, which clearly indicates the open slit porous

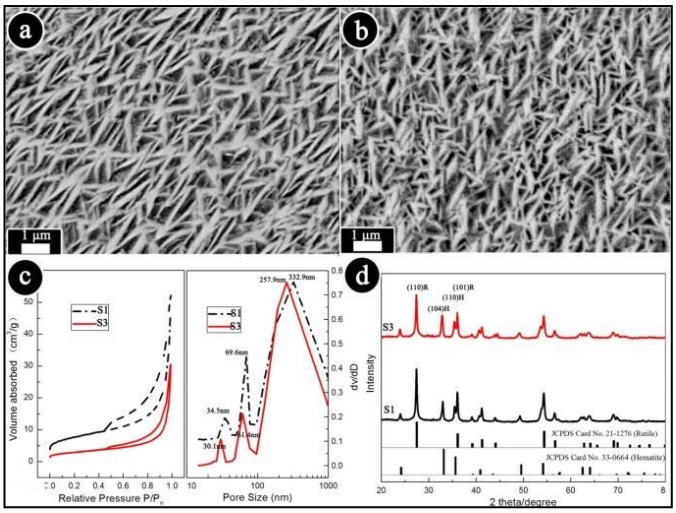


Fig. 2 Integrated characterizations of the as-obtained meso-macroporous $TiO_2$-$Fe_2O_3$ composite particles in Table 1. The cross-section images of the S1: (a), S3: (b), (c) Nitrogen adsorption–desorption isotherms and the corresponding pore size distribution, (d) XRD patterns.

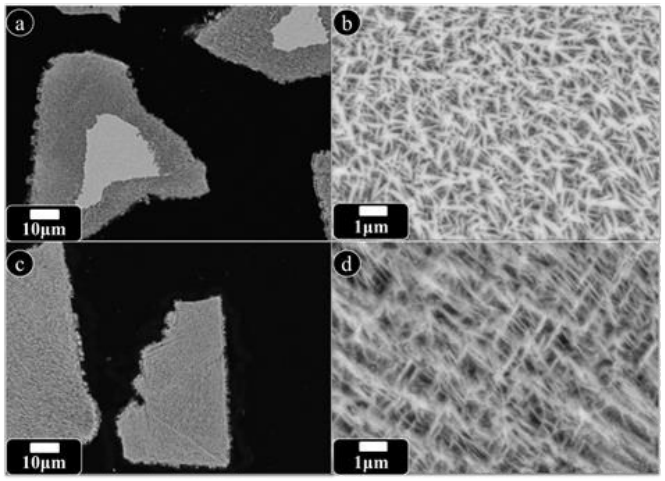


Fig. 3 SEM images of the cross-section of sample S4 (a-b) and S5 (c-d) in table 1.

structure with conical geometry. The pore size distribution of the as-synthesized sample calculated from the BJH desorption isotherm shows a hierarchical pore size distribution from meso to macropores(17.2nm-25.4nm, 39.9nm-62.4nm and 87.5nm-373.9nm). This is in good agreements with the SEM and TEM results and confirms the meso-macro complex porous structure of the products which is formed by ordered arrange of laminary $TiO_2$ nanocrystals. The BET specific surface areas and pore volumes are 76.5$m^2$ $g^{-1}$ and 0.47 $cm^3$ $g^{-1}$, respectively. Fig. 1h shows the X-ray diffraction (XRD) pattern of the porous composite particles. The narrow sharp peaks suggest that the products are high crystalline, which agrees well with the HRTEM results. The main crystal phases of the product are $TiO_2$ (rutile) and $Fe_2O_3$ (Hematite), no characteristic peaks of impurities are detected. It should be noted that the diffraction intensity ratio of (101)R to (110)R is obviously larger compared with the standard card(Table 1), which may be attributed to the special fractional crystallization progress of the ilmenite and will be discussed in detail in the formation mechanism section. EDX spectrum (Fig. 1i) is also carried out to further reveal the composition of the product, which indicates the existence of Ti, Fe and O. In addition, XRF analysis also confirms Ti, O and Fe as the main elements (97.2% of the products) (see Fig. S5 and Table S1).

It should be noted that, by simply changing the reduction time, porous particles with different specific surface areas and pore sizes can be obtained (Fig. 2a,b and Table 1). With the decrease of the reduction time from 15min to 5min, the pore size increases while the BET specific surface area decreases (Fig 2a, 2c and Table1). In addition, with the increased reduction time from 15min to 30min, the pore size gets larger while the BET specific surface area decreases (Fig 2b, 2c Table 1). Meanwhile, it is found that all the samples obtained with different reduction duration possess type IV N2 adsorption-desorption isotherms with D kind hysteresis loops (Fig 2c), which indicates the open slit porous structure with conical geometry.

The XRD patterns of the samples S1 and S3 obtained at different reduction time are shown in Fig. 2d, similar with sample S2, sample S1 and S3 are also composed of $TiO_2$(rutile) and $Fe_2O_3$(Hematite). The enhanced diffraction intensity ratio of (101)R to (110)R can also been seen (Table 1). Moreover, the XRF results reveals that the Fe content in the products decreases gradually in the order S1>S2>S3, revealing that the reduction treatment enhances the leach ability of ferrous phase (see Fig S5 and Table S1).

To further study the influence of reduction treatment on the structure of the products, contrast experiments without reduction treatment (S4 in table 1) and with extended reduction time of 45min (S5 in table 1) have also been carried out, respectively. Fig. 3a-b is a panoramic SEM image of the cross section of the S4, from which it can be seen that a large amount of Fe-containing phase exists in the central part of the particle. Comparatively, the sample S5 (Fig. 3c-d) possesses uniform pore structure through the whole particles. It can be seen from panel b and d that, compared to those obtained with moderate reduction time, $TiO_2$ crystals are relatively thicker in S4 and thinner in S5, respectively, both of which lead to decreased porosity. From the above mentioned results, it can be concluded that the reduction treatment can make the structure of the intermediate particles unconsolidated and favors the elimination of Fe-containing phase in the leaching process. On the other hand, a properly elongated reduction duration (from 0 to 15min) favors the increase of the porosity, but a further elongated reduction duration (from 15 to 45min) will cause the demolishment of the $TiO_2$ framework and reduce the porosity.

**The formation mechanism of discussion.**

**The Formation of flaky $TiO_2$ crystals.** From the above mentioned SEM, TEM and BET analysis, it can be concluded that the porous structure of the products are arranged by laminary $TiO_2$ crystals in a layer-by-layer manner with short range order. According to the XRD results (Table 1), the diffraction intensity ratio of (101)R to (110)R is obviously larger

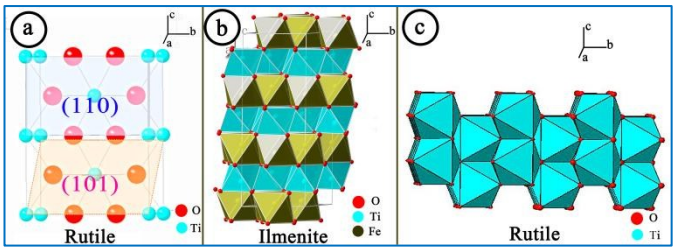


Fig. 4 Sketch of crystal structures. (a) crystal cells of rutile, (b) octahedral structure of ilmenite, (c) octahedral structure of rutile.

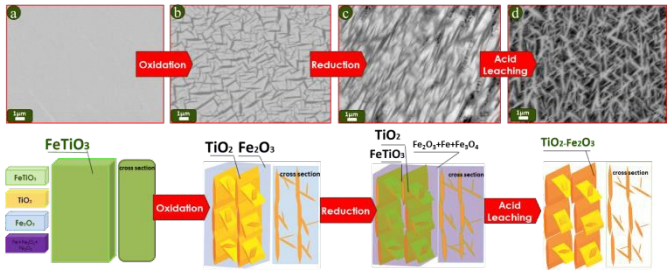


Fig. 5 Schematic illustration of the possible formation process of the $TiO_2$-$Fe_2O_3$ composite porous structure. (a-d) SEM images of the products obtained at different reaction stages: a raw ilmenite, b after oxidation treatment, c after reduction treatment, d after acid leaching.

compared with the standard card, which indicates that the laminary rutile phase tends to extend along crystal axis b, and the growth in axis c is hampered (Fig. 4a). The formation of the special flaky $TiO_2$ crystals may depends strongly on the crystalline structure of the ilmenite (as the raw material in the present study). From Fig. 4b, it can be seen that the TiO octahedron and FeO octahedron staking layer-by-layer along crystal axis c in ilmenite crystal cell. In the fractional crystallization process (during heat treatment), $TiO_2$ nanocrystals are formed in a manner of hampered growth in c axis (by FeO). Therefore, the extension of the newly formed $TiO_2$ nanocrystals are more favored to occur along b axis (Fig. 4c), which leads to the increased diffraction strength of (101) crystal plane of $TiO_2$ in the XRD pattern.

**The formation mechanism of the $TiO_2$-$Fe_2O_3$ porous composite.** To understand the formation process of the $TiO_2$-$Fe_2O_3$ composite porous structures, SEM observations of the products at different reaction stages have been carried out(Fig. 5). The possible formation processes and the SEM images of the particles obtained at different reaction stages are shown in Figure 6. At the initial step, the ilmenite particle indicates the uniform and compact nature of its inner section (Fig. 5a). After oxidation for 40min (Fig. 6a), the particles remain compact and a continuous frame of well distributed flake-like $TiO_2$ nanocrystals (dark phase in Fig. 5b) can be observed with destroyed by the formation of pores and new crystal phases. As can be seen in Fig. 5c, the frame of $TiO_2$ (dark phase) get more concentrated and the boundary between the $TiO_2$ and the $Fe_2O_3$ (bright phase) become obscure, which indicates that a recombination reaction (Fig. 6b, Fig. S6b) occurs on the

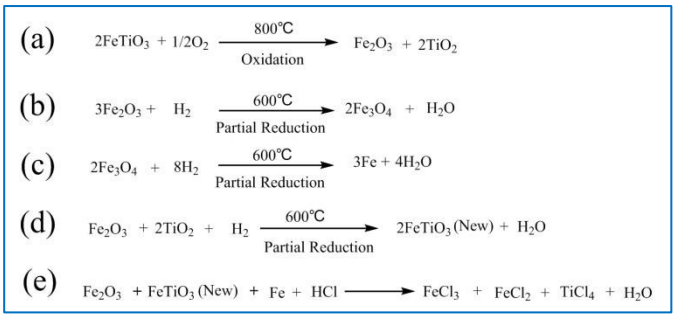


Fig. 6 The chemical reactions involved in the preparation of $TiO_2$-$Fe_2O_3$ composites.

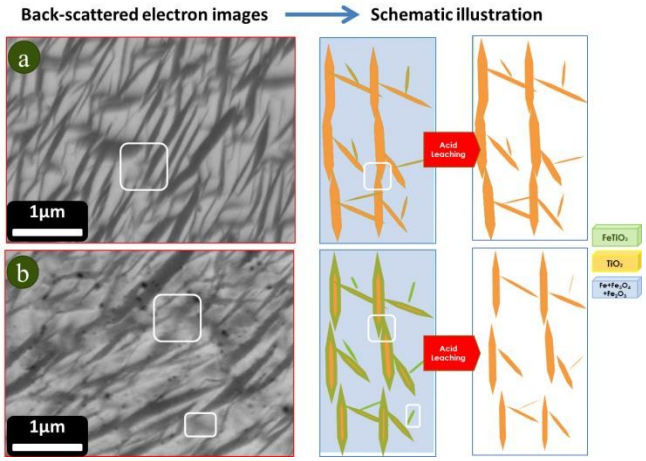


Fig. 7 Schematic illustration of the control over the pore structure of the $TiO_2$-$Fe_2O_3$ composites, and high-magnification back-scattered electron images taken on the the cross-section of the samples obtained by reduction at 600℃ for (a)5min and (b)30min.

interface of the $TiO_2$ and $Fe_2O_3$ phases (formed previously in the oxidation process). In addition, from the low-magnification SEM image of the particles (Fig. S7), a new Fe phase (the bright particle-like phase) is formed through the reduction of $Fe_2O_3$ (Fig. 6c,d, Fig. S7). According to the results of Zhang's work[37], at a lower reduction temperature of 600℃, the recombination reaction is in a low degree and the marginal $FeTiO_3$ phase formed thereof can be easily eliminated by acid leaching. This controllable recombination reaction provides an effective way to tailor the pore structure of the $TiO_2$ frame without destroying its overall structure. Finally, porous structure can be obtained by acid leaching, in which most of the ferrous phase is eliminated (Fig. 6e). In the leaching treatment of the particles obtained after oxidation and reduction, all the $FeTiO_3$ phase (low content) and a controlled part of the $Fe_2O_3$ phase (high content) are leached out, resulting in $Fe_2O_3$ doped porous $TiO_2$ product(Fig. 5d).

**Channel regulation mechanism.** Contrast experiments with various reduction times have been carried out to further understand the effect of the reduction process on the pore structure (Fig. 7). As shown in Fig. S8a, with a short reduction time of 5min, the iron phase is formed by reducing reaction occurred mainly on the surface of the composite

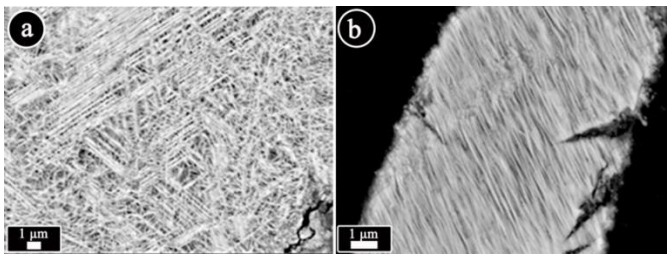


Fig. 8 (a, b) SEM images of the cross-section of sample S2 (minor particles with high degree of order of pores).

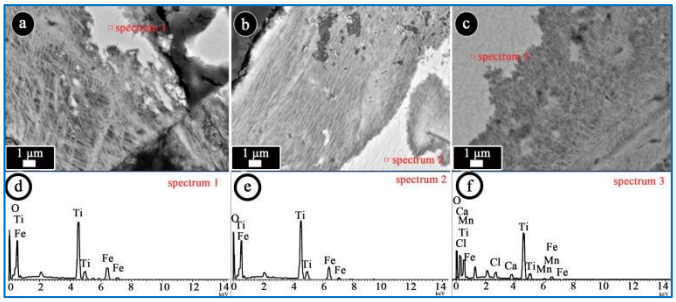


Fig. 9 Integrated characterizations of the partly leached composite particles (obtained by stepwise treating of ilmenite: (a) oxidized at 800℃ for 40min, (b) reduced at 600℃ for 15min, (c) leached for 1h): (a–c) SEM images of the cross-section of the samples, (d–f) EDX spectra of the corresponding particles.

particles. In the inner section of the particle (Fig. 7a), only a tiny slight reaction between $TiO_2$ and $Fe_2O_3$ can be observed, as is marked by the white square in Fig.7a. Therefore, with short reduction time, the preformed $TiO_2$ framework is barely affected. Fig. 7b is the SEM image of the inner section of a typical particle obtained after reduction for a elongated duration of 30min, which reveals that the reduction reaction spreads out and the iron phase and pores exist all over the particle (see Fig. S8b). Compared with the sample obtained with a reduction time of 15min, the extent of the recombination reaction between $TiO_2$ and $Fe_2O_3$ gets larger and some fine $TiO_2$ crystallites are consumed, which lead to the reduction of both pore content and specific surface area.

**Order degree control of the pores.** In addition to rutile $TiO_2$ morphology, it is also found that the order degree of porous structure can be controlled by the degree of crystallinity of initial ilmenite. We have observed that product particles with different degree of order coexist in the same sample. For instance, in sample S2, most particles possess pore morphology similar to that shown in Fig.1, but some particles with higher degree of pore order can also be seen, as is shown in Fig. 8a and b (the typical case). This may be attributed to the fact that in the natural formation process of ilmenite, the degree of lattice order may not be uniform in different position of ilmenite ores because of the different contents of impurity elements. Since the ilmenite particles as the initial material are prepared through pulverization of large ores, particles with lower impurity elements content possess higher degree of lattice order[38]. To further understand the relationship between the crystallinity of raw ilmenite and the

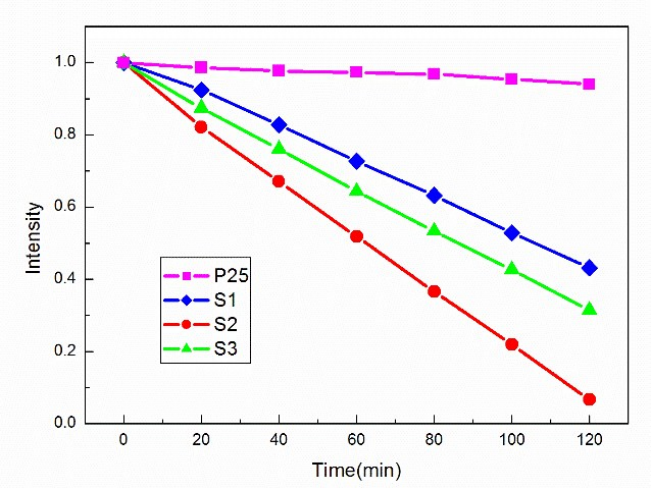


Fig. 10 Photocatalytic degradation curves of MB on the porous $TiO_2$-$Fe_2O_3$ samples and P25 under visible light irradiation.

degree of order of the final products, partial leaching treatment has been carried out by shortening the leaching duration. The partially leached particles have both porous $TiO_2$-$Fe_2O_3$ section (leached entirely) and mixture section (without leaching), which make it possible to analyze both the pore structure and the composition of the unleached section. SEM images of the cross section of different particles from the same sample (obtained by oxidization at 800℃ for 40min-reduction at 600℃ for 15min-leaching for 1h)(Fig. 9a-c) and the corresponding EDX spectra taken at the unleached section are shown in Fig. 9d-e. It can be seen that particles with high degree of pore order (Fig. 9a and b) have relatively simple composition (only Fe, Ti and O elements are detected, as shown in Fig. 9d and e. On the other hand, the particles with low degree of pore order possess much complex composition (Fig. 9c and f) with some impure elements. From these results, it can be concluded that the existence of impurity may lead to low degree of crystallinity of raw ilmenite, which further results in low degree of pore order for the final porous $TiO_2$-$Fe_2O_3$ composites.

**Photocatalytic properties.** Methylene blue (MB), a common toxic azo dye in colored wastewater, is selected as a model pollutant for photocatalytic oxidation performance of the porous $TiO_2$-$Fe_2O_3$ products. Figure 10 describes the activity of the as-prepared meso-macroporous $TiO_2$-$Fe_2O_3$ samples under visible light. The as prepared samples possess certain photocatalytic activities, which is much better than commercial P25. The reason for the improved visible light photocatalytic activity lies in the high absorption ratio of the meso-macroporous $TiO_2$-$Fe_2O_3$ samples (Fig. S9), which can be attributed to the existence of $Fe_2O_3$[29] (possesses much lower band gap than $TiO_2$). The degradation rate of MB on different samples follows the order: S2>S3>S1, which agrees well with the order of BET surface area (Table 1). It should be noted that sample S2 possesses the best catalytic activity among the three samples under consideration, which can be attributed to the combination of large surface area, suitable light absorption and band gap energy, the highest surface hydroxyl oxygen

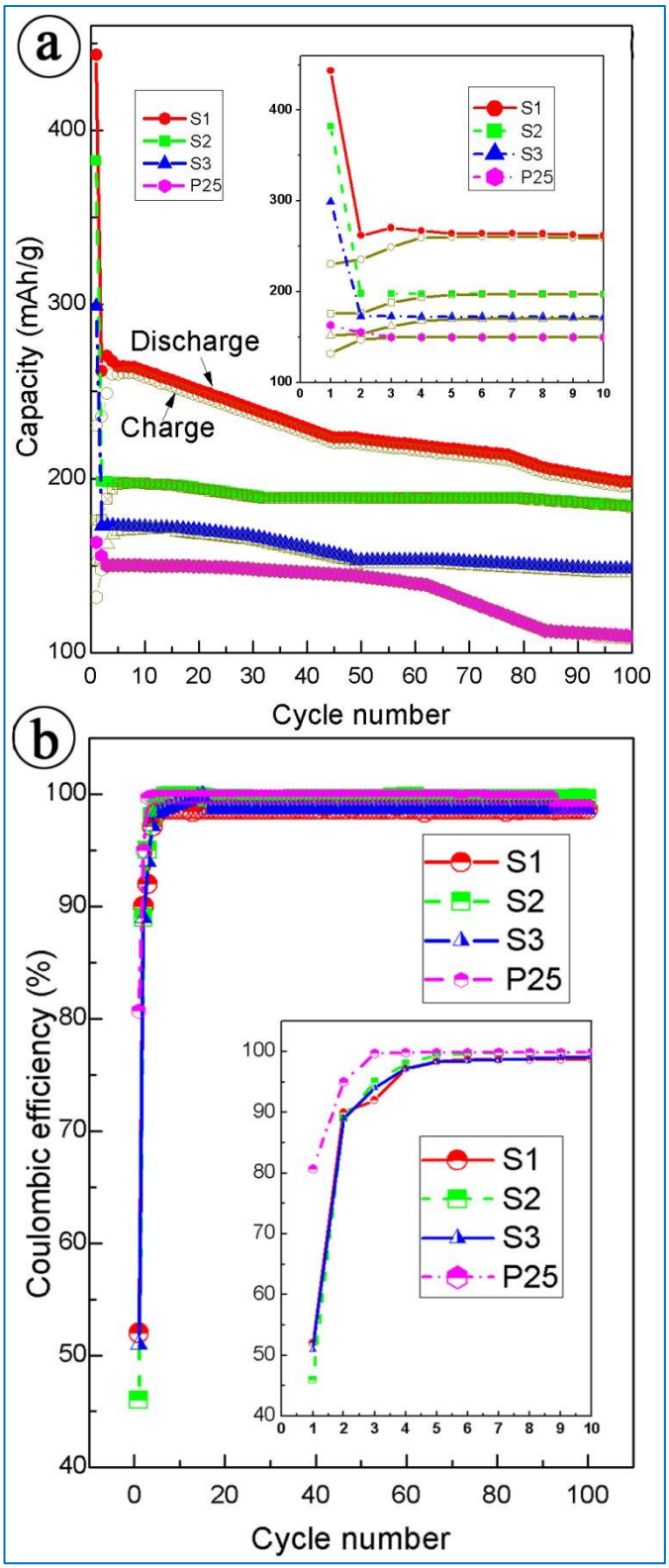


Fig. 11. Capacity versus cycle number plots (a) and coulombic efficiency versus cycle number plots (b) of P25 and different $TiO_2$-$Fe_2O_3$ composites samples, cycled in the voltage range of 1.0-3.0V at current density of 0.2mA • $cm^{-2}$. Insets are the enlarged view of the corresponding plot in the first ten circles.

content[39], and the lowest $Ti^{3+}$ content[36](see the xps date in Fig. S10 and Table S2).

**Electrochemical performance of the porous $TiO_2$-$Fe_2O_3$ composites as anode materials for lithium-ion batteries.** The electrochemical characteristics of the as-prepared $TiO_2$-$Fe_2O_3$ composites and P25 have been evaluated using two-electrode coin-type cells. Fig.11 shows the discharge/charge capacities and the corresponding coulombic efficiencies of different samples at a current density of 0.2mA·$cm^{-2}$. It can be seen that the $Li^+$ storage performances of the $TiO_2$-$Fe_2O_3$ composites are significantly improved compared with that of P25 (see Fig.11a and Table S3). The high capacity may be attributed to the existence of α-$Fe_2O_3$ component, which possesses a much higher theoretic capacity of ca. 1007mAh·$g^{-1}$[40]. The capacity gets higher with the increased iron oxide content (S1>S2>S3), however, high Fe content also leads to inferior cycling stability. On the other hand, despite the high discharge/charge capacities, the porous composites exhibit initial low coulombic efficiencies of 52%, 46% and 51% for S1, S2 and S3, respectively(Figure 11b and Table S3), indicating a large irreversible capacity. The irreversible capacity may be ascribed to the commonly believed phenomenon that the rich surface defects and vacancies of porous materials (with relatively high specific surface areas) usually lead to irreversible lithium storage [41-42] and relatively low coulombic efficiency thereof. It is worthy noting that, from the second to the 100th cycle, excellent cyclic stabilities are observed for the three samples (i. e., the capacities decrease slowly with the increased cycling number, especially for sample S2). Furthermore, the coulombic efficiency rapidly increases to 95% during the first four cycles and stays at a high level (almost 100%) in the subsequent cycles (Fig. 11b). Considering the good electrochemical properties, the $TiO_2$-$Fe_2O_3$ composites possess considerable potential for use as an alternative anode material for lithium ion batteries.

## Conclusions

A novel heat treatment induced fractional crystallization strategy has been developed for cost-effective and large scale preparation of meso-macroporous $TiO_2$-$Fe_2O_3$ composite particles using naturally abundant ilmenite as the initial material. The products are formed through fluid-bed roasting and acid leaching process and their pore structure and composition have been found to be tunable simply by controlling the reaction parameters, such as the roasting time, temperature, precursor particle size, and post-roasting treatment. It is found that the synergism of porous structure and doping of α-$Fe_2O_3$ leads to improved photocatalytic and electrochemical performances of the porous $TiO_2$-$Fe_2O_3$ composites. Our works provides a new strategy for reasonable combination of low cost raw material, large scale fabricating process and fine control over the structure and composition in the design and preparation of functional materials. We believe such a synthetic strategy holds the potential to be extended for the preparation of other composite structures from either

natural or well-designed precursors in a cost-effective and industrial acceptable manner.

## Acknowledgements

This project was supported by the China Postdoctoral Science Foundation (2015M571127) and by National Outstanding Youth Science Fund Project of NSFC (Grant No. of 21325628).

## Notes and references

1 D. Fattakhova-Rohlfing, A. Zaleska, and T. Bein, *Chem. Rev.* 2014, **114,** 9487-9558.
2 M. B. Dickerson, K. H. Sandhage and R. R. Naik, *Chem. Rev.* 2008, **108,** 4935-4978.
3 C. Boissiere, D. Grosso, A. Chaumonnot, L. Nicole and C. Sanchez, *Adv. Mater.* 2011, **23,** 599-623.
4 P. Innocenzi and L. Malfatti, *Chem. Soc. Rev.* 2013, **42,** 4198-4216.
5 B. Zhao, R. Cai, S. Jiang, Y. Sha and Z. Shao, *Electrochimica Acta* 2012, **85,** 636-643.
6 E. L. Crepaldi, G. Soler-Illia, D. Grosso, F. Cagnol, F. Ribot and C. Sanchez, *J. Am. Chem. Soc.* 2003, **125,** 9770-9786.
7 S. Y. Choi, M. Mamak, N. Coombs, N. Chopra and G. A. Ozin, *AdV. Funct. Mater.* 2004, **14,** 335-344.
8 D. G. Shchukin and R. Caruso, *AdV. Funct. Mater.* 2003, **13,** 789-794.
9 W. Sun, S. Zhou, B. You and L. Wu, *Chem. Mater.* 2012, **24,** 3800-3810.
10 G. Calleja, D. P. Serrano, R. Sanz and P. Pizarro, *Microporous Mesoporous Mater.* 2008, **111,** 429-440.
11 A. Mitra, A. Bhaumik and B. K. Paul, *Microporous Mesoporous Mater.* 2008, **109,** 66-72.
12 S. Yuan, Q. R. Sheng, J. L. Zhang, H. Yamashita and D. N. He, *Microporous Mesoporous Mater.* 2008, **110,** 501-507.
13 C. S. Chao, K. H. Liu, W. L. Tung, S. Y. Chen, D. M. Liu and Y. P. Chang, *Microporous Mesoporous Mater.* 2012, **152,** 58-63.
14 S. X. Luo, F. M. Wang, Z. S. Shi and F. Xin, *J. Sol-Gel Sci. Technol.* 2009, **52(1),** 1-7.
15 Z. Zhang, C. Wang, C. R. Zakaria and J. Y. Ying, *J. Phys. Chem. B* 1998, **102,** 10871-10878.
16 Y. Murakami, T. Matsumoto and Y. Takasu, *J. Phys. Chem. B* 1999, **103,** 1836-1840.
17 P. Raveendran, M. Eswaramoorthy, U. Bindu, M. Chatterjee, Y. Hakuta and H. Kawanami, *J. Phys. Chem. C* 2008, **112,** 20007-20011.
18 L. Zhou and P. O'Brien, *Phys. Status Solidi A*, 2008, **205,** 2317-2323.
19 K. Du, D. Yang and Y. Sun, *Ind Eng Chem Res.* 2009, **48,** 755-762.
20 M. E. Davis, *Nature*, 2002, **417,** 813-821.
21 Y. Han, D. Li and L. Zhao, *Angew. Chem. Int. Ed.* 2003, **42,** 3633-3637.
22 J. W. Cahn and J. E. Hillard. *J. Chem. Phys.* 1958, **28,** 258-267.
23 J .W. Cahn and R. Charles, J. *Phys.Chem.Glasses.* 1965, **6,** 181-182.
24 L. Qin, X. Pan, L. Wang, X. Sun, G. Zhang and X. Guo, *Appl. Catal. B: Environ.* 2014, **150-151,** 544-553.
25 J. Thomas and M. Yoon, *Appl. Catal. B: Environ.* 2012, **111-112,** 502-508.
26 A. Naldoni, M. D'Arienzo, M. Altomare, M. Marelli, R. Scotti, F. Morazzoni and E. Selli, *Appl. Catal. B: Environ.* 2013, **130-131,** 239-248.
27 N. Farhangi, R. R. Chowdhury, Y. Medina-Gonzalez, M. B. Ray and P. A. Charpentier, *Appl. Catal. B: Environ.* 2011, **110,** 25-32.
28 A. Ghicov and P. Schmuki, *Chem. Commun.* 2009, 2791-2808.
29 H. Tang, D. Zhang, G. Tang, X. Ji, W. Li and C. Li, *Ceramics International* 2013, **39,** 8633-8640.
30 W. Wang, F. Bu and J. S. Jiang, *Mater. Lett.* 2015, **139,** 89-92.
31 Z. Z. Djuric, O. S. Aleksic, M. V. Nikolic, N. Labus, M. Radovanovic and M. D. Lukovic, *Ceramics International* 2014, **40,** 15131-15141.
32 B. Palanisamy, C. M. Babu, B. Sundaravel, S. Anandan and V. Murugesan, *J. Hazardous Mater.* 2013, **252,** 233-238.
33 S. J. Hu, *Zhejiang university of technology for the degree of master* 2011.
34 Y. M. Zhao, L. G. Tang, Z. F. Luo, C. Liang, H. Xing and C. L. Duan, *Sep. Sci. Technol.* 2012, **47,** 2256-2261.
35 C. Sheng, Y. Zhao, C. Duan, B. Zhang, P. Feng and K. Lv, *Procedia Engineering* 2015, **102,** 1546-1554.
36 L. Li and C. Y. Liu, *Eur. J. Inorg. Chem.* 2009, 3727-3733.
37 J. B. Zhang, G. Y. Zhang, Q. S. Zhu, C. Lei, Z. H. Xie and H. Z. Li, *Metallurgical and Mater. Transactions B* 2014, **45(3),** 914-922.
38 K. S. Deffeyes, F. J. Lucia and P. K. Weyl, *Soc. Econ Paleont Miner Spec Publ.* 1965, **13,** 71-88.
39 Y. Nosaka, S. Komori, K. Yawata, T. Hirakawa and A.Y. Nosaka, *Phys. Chem. Chem. Phys*. 2003, **5,** 4731-4735.
40 X. L. Wu, Y. G. Guo, L. J. Wan and C. W. Hu, *J. Phys. Chem. C* 2008, **112,** 16824-16829.
41 C. Zhao, L. J. Liu, Q. Y. Zhang, J. Rogers, H. L. Zhao and Y. Li, *Electrochimica Acta* 2015, **155**, 288-296.
42 Z.Y. Wang and X.W. Lou, *Adv. Mater.* 2012, **24**, 4124-4129.

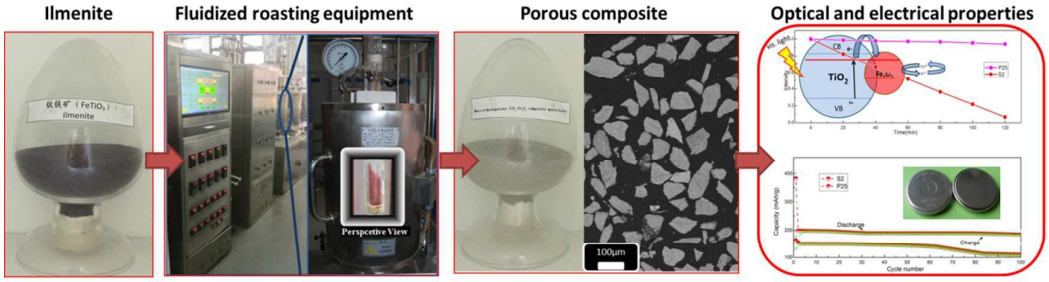


**Meso-macroporous $TiO_2$-$Fe_2O_3$ composites with tunable structure and property were prepared via a heat-treatment induced fractional crystallization strategy in fluidized bed.**